Rare Metal Materials and Engineering
Volume**, Issue ***, ****
Available online at **www.rmme.ac.cn**

Science Press

Cite this article as: Rare Metal Materials and Engineering,

ARTICLE

DOI: 10.12442/j.issn.1002-185X.20250091

Microstructure and thermal properties of $MoSi_2$ and $Gd_2Zr_2O_7$ composite coatings on Mo-Re alloy

Chong Zhang[1, *], Xin Wang [1], Hailong Xu [1], Yanchao Li [1], Tongxiang Ma [1], Shaopeng Wang [1, *]

[1] *Northwest Institute for Nonferrous Metal Research, Xi'an 710016, China*

Abstract: Dual-layer thermal barrier coatings with ultra-high temperature resistance were prepared on the surface of molybdenum-rhenium alloy hot-end components. The preparation of the $MoSi_2$- $Gd_2Zr_2O_7$ dual-layer thermal barrier coatings was designed based on the coefficient of thermal expansion and coatings functionality and completed using atmospheric plasma spraying technology. The microstructure, mechanical properties, and thermal properties were analyzed. The results indicate that the adhesion of the prepared double-layer composite thermal barrier coatings is excellent, and no noticeable cracks appear at the interface. Compared to $MoSi_2$ coatings with a low fracture toughness (0.88 $MPa\cdot m^{1/2}$), $Gd_2Zr_2O_7$ coatings exhibits higher fracture toughness (1.74 $MPa\cdot m^{1/2}$) and stronger resistance to crack propagation. The prepared $MoSi_2$- $Gd_2Zr_2O_7$ composite coatings has a high porosity rate (39%), low thermal conductivity (1.02 W/m·K, 1200°C), and low thermal diffusivity (0.249 mm^2/s, 1200°C). Additionally, it possesses a high oxygen vacancy concentration, resulting in a lower thermal diffusivity/thermal conductivity ratio, ensuring excellent insulation performance.

Key words: $MoSi_2$- $Gd_2Zr_2O_7$ coatings; Molybdenum-rhenium alloys; TBCs; Thermal insulation performance

Molybdenum-rhenium alloys (Mo-Re) are extensively utilized in aerospace, nuclear, and military applications due to their exceptional radiation resistance, high tensile strength, favorable flexibility, and robust thermal shock resistance [1]. They are employed in the fabrication of engine nozzles, combustion chamber liners, and other critical military components [2-4]. To enable operation at ultra-high temperatures (>1700K), thermal barrier coatings (TBCs) must be applied to the alloy surface. However, traditional plasma-sprayed YSZ is limited to working environments below 1400 K due to its phase transformation (t'→t+c) [5-7] at elevated temperatures. Consequently, it is essential to develop a heat-insulating coatings material characterized by superior thermal insulation properties and a high phase-change temperature to address the issue of inadequate service temperatures for molybdenum-rhenium alloys.

Among the rare earth zirconates ($RE_2Zr_2O_7$), gadolinium zirconate ($Gd_2Zr_2O_7$, GZ) exhibiting a crocolite structure demonstrates significant phase stability, with the transition to a defective fluorite structure occurring at 1550°C. Additionally, its thermal conductivity was lower than that of YSZ [8-10]. However, the significant mismatch in thermal expansion coefficients between the coatings and substrate adversely affected the mechanical properties of the Mo-Re alloy GZ coatings, leading to inadequate thermal shock resistance [11-13]. This limitation significantly restricted the high-performance applica-

Received date:
Foundation item: The work is sponsored by scientific and technological innovation of Shaanxi provincial state-owned capital operation budget (2022-056), Institute's Self-developed Technology Programs (0801YK2317), Qin Chuangyuan Cites High-level Innovation and Entrepreneurship Talent Programs (QCYRCXM-2023-120), Qinchuang Original Industry Cluster Zone 'Four Chains' Integration Programs (2024CY-JJQ-46), National Natural Science Foundation of China (52071274), Key Research and Development Projects of Shaanxi Province (2023-YBGY-442), Science and Technology Nova Project - Innovative Talent Promotion Program of Shaanxi Province (2020KJXX-062).
Corresponding author: Chong Zhang, M.E., Assistant Engineer, Northwest Institute for Nonferrous Metal Research, Xi'an 710016, P. R. China, Tel: 0086-29-86283410, E-mail: zhangchong0411@163.com
Shangpeng Wang, Ph.D., Professor, Northwest Institute for Nonferrous Metal Research, Xi'an 710016, P. R. China, Tel: 0086-29-86230194, E-mail: pengfly239@163.com

tion of the GZ coatings on Mo-Re alloys. Consequently, selecting an appropriate bonding layer that effectively matches the thermal expansion coefficients between the substrate and top layer is essential.

The $MoSi_2$ coatings exhibited a high melting point, moderate density, and outstanding overall performance in silicide coatings' materials [14-16]. During high-temperature oxidation, the volatile oxidation product MoO_3 evaporated promptly, enabling the formation of a complete and continuous SiO_2 protective film on the surface of $MoSi_2$ that effectively inhibited oxygen diffusion[17-19]. Consequently, it was regarded as an up-and-coming candidate for high-temperature protective coatings applications [20-22]. Additionally, the thermal expansion coefficient of $MoSi_2$ (9.2×10^{-6} K^{-1}) lies between that of the base Mo-Re alloy (7.5×10^{-6} K^{-1}) and the GZ coatings (10.4×10^{-6} K^{-1}) [23-25] utilized in this study, allowing $MoSi_2$ to function both as an anti-oxidation coatings and as an adhesive phase for GZ.

To address the challenges associated with preparing a GZ coatings on the surface of a molybdenum-rhenium alloy, this study adopted a coatings' design approach and employed atmospheric plasma spraying to fabricate $MoSi_2$-GZ coatings. The microstructure and performance of the thermal barrier coatings (TBCs) were thoroughly characterized. This research is anticipated to offer valuable insights into the high-performance application of $MoSi_2$-GZ coatings on molybdenum-rhenium alloys.

1 Experiment

1.1 Preparation of substrate and coatings

Molybdenum-rhenium alloys measuring $\Phi 25.2 \times 3$ mm^3 were used as the substrates. They were obtained from alloy rods by wire-electrode cutting. $MoSi_2$ (the powders provided by BEIJING SUNSPRAYING NEW MATERIAL CO., LTD.) coatings with about 50 μm was respectively fabricated on the substrate as bond layers by air plasma spray (APS, SG-100, Praxair S.T., America) with commercial powders. The information of $MoSi_2$ and $Gd_2Zr_2O_7$ powder was shown in Table 1. The top coating of $Gd_2Zr_2O_7$ (referred to as GZ, with about 300 μm) (the powders provided by BEIJING SUNSPRAYING NEW MATERIAL CO., LTD.) was deposited via air plasma spray (APS, SG-100, Praxair S.T., Americra) with the powder synthesized by solid-state reaction as shown in Fig. 1. The deposition parameters were optimized using the Box-Behnken Design (BBD) method [26] and the detail spray parameters were shown in Table 2. Following the coatings deposition, specimens were heat-treated at 600 °C for 1 h in an argon atmosphere furnace to diminish the residual stress.

Table 1 The information of $MoSi_2$ and $Gd_2Zr_2O_7$ powder.

Powder	Granularity (μm) D10-D50-D90	Loose specific weight (s/cm^3)	Powder fluidity (s/50g)
$MoSi_2$	29.5-47.1-73.3	1.56	40.54
$Gd_2Zr_2O_7$	32.5-46.3-65.4	2.06	24.67

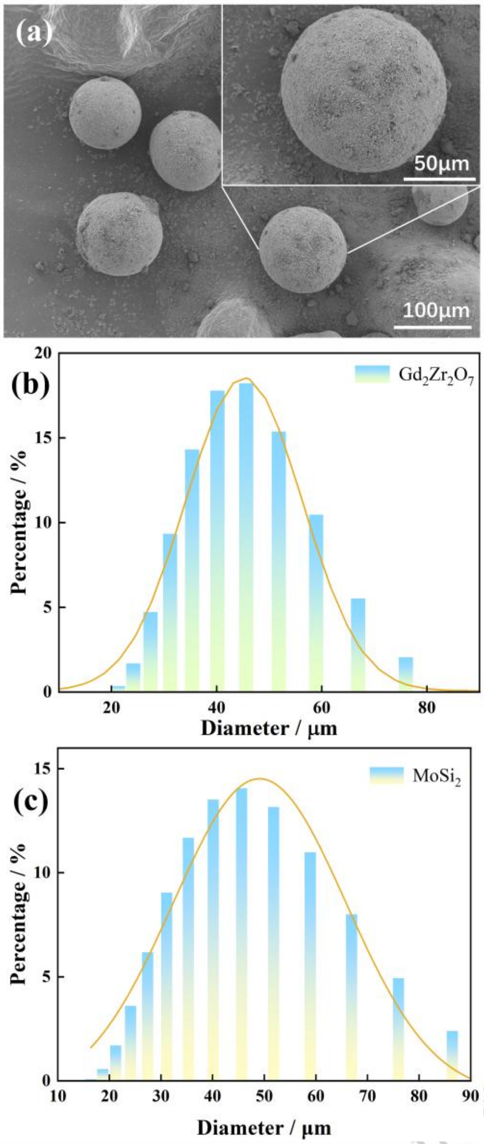

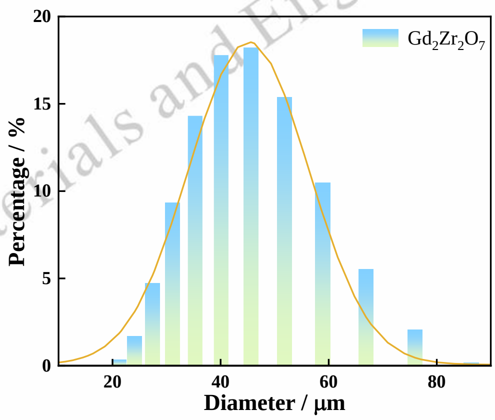

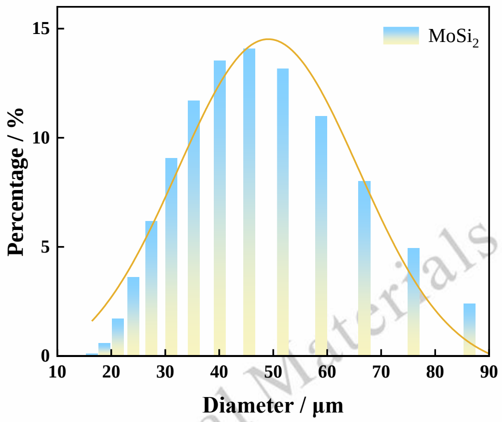

Fig.1 SEM morphological image of $Gd_2Zr_2O_7$ powder and the granularity of the $MoSi_2$ and $Gd_2Zr_2O_7$ powder.

Table 2 Spray parameters of the top coatings (GZ) and the bond coatings （$MoSi_2$）.

Spraying Parameter	Value	
	$MoSi_2$	GZ
Spray distance (mm)	100	100
Primary gas Ar (slpm)	104	90
Second gas H_2 (slpm)	3	4
Carrier argon gas flow rate (slpm)	12	12
Volts (V)	40	45
Current (A)	750	850
Powder feed rate (rpm)	2	2
Gun traverse speed (mm/s)	700	700

1.2 Microstructure and phase composition

The cross-sectional morphology, and elemental content of the as-sprayed coatings were analyzed using scanning electron microscopy (SEM, Hitachi SU5000, Japan) equipped with an INCA-AE350 energy-dispersive spectrometer (EDS). Phase compositions were determined by x-ray diffraction (XRD, SmartLab 9kW, Japan), which was conducted on a Rigaku x-ray diffractometer with Cu-Kα (λ= 1.5418°) radiation.

1.3 Evaluation of Coatings Performance

The coatings' microhardness was evaluated on a polished cross-surface using Vickers indentation testing (HVS-1000) with a load of 200 g (≈2 N) and a dwell time of 15 s. The average microhardness was determined by repeating the measurement ten times and excluding the maximum and minimum values [27].

To measure the fracture toughness of GZ coatings, Vickers indenter with a load of 1N was utilized to create the appropriate cracks on the polished cross-section of coatings [28]. According to the Evans & Wilshaw model, the fracture toughness could be calculated by the following equation:

$$K_{IC} = 0.079\left(\frac{P}{a^{3/2}}\right) log\frac{4.5a}{c} \quad (1)$$

where K_{IC} is the fracture toughness (MPa·m$^{1/2}$), P is the load of the indenter (N), c is the length from the tip of cracks to the center of indentation (m), and a is the half-length of diagonal (m) [29,30].

The porosity of the coatings was quantified through the analysis of cross-sectional SEM images using Image Pro Plus software. The bond strength of the coatings was evaluated through tensile testing in accordance with established standards (GB T 8642-2002).

Simultaneously, the specific heat capacity of $MoSi_2$-GZ coatings was measured by the DSC method (LFA 467, NETZSCH, Germany), and the thermal conductivity and diffusivity were detected using free-standing samples with dimensions 10mm × 10mm × 1.19 mm.

2 Results and Discussion

2.1 Microstructure of the $MoSi_2$-$Gd_2Zr_2O_7$ coatings

The surface morphologies of the $MoSi_2$ bonding layer and the $Gd_2Zr_2O_7$ top layer were shown in Fig. 2. The $MoSi_2$ layer was not polished to improve the bonding strength of the coating. The splashed droplets on the surface, lamellar stacking, and microcracks in the coating could still be observed. Although the layered characteristics of the $Gd_2Zr_2O_7$ top layer were not obvious after surface polishing, pores within the coating remained visible.

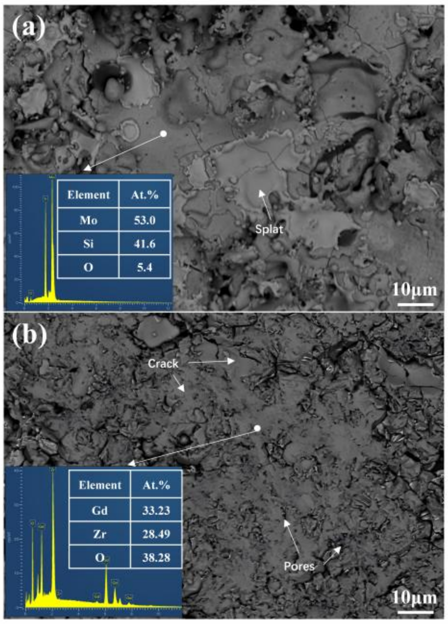

Fig.2 Microstructure and structure analysis of the surface of $MoSi_2$ and GZ coatings. (a) $MoSi_2$ coatings. (b) $MoSi_2$-GZ coatings.

The cross-sectional microstructures of the Mo-Re alloy surface coated with $MoSi_2$ and GZ were shown in Fig. 3. Herein, Fig. 3(a) presented the entire cross-sectional morphology of the coatings. The overall thickness of the coating approximated 350 μm, featuring a $MoSi_2$ thickness of approximately 50 μm and a GZ thickness of 300 μm. It could be observed that the coatings were firmly bonded to the substrate, and no extensive horizontal and vertical cracks or peeling were present on the entire coatings. In the magnified view of Fig. 3(a), it could be observed that the interface bonding at the contact region with the external surroundings remains excellent, and the minute cracks might be attributed to the damage incurred to the coatings sample during wire cutting.

By zooming in on specific regions of Fig. 3(a), Fig. 3(b), (c), and (d) were acquired for further characterization. The porosity thickness of the coatings was analyzed via Image pro plus software for Fig. 3(b), with a porosity of 39%. In Fig. 3, it was observed that a large-scale porous area and a small portion of semi-molten regions existed in the GZ surface layer. When magnifying the semi-molten region, it was revealed that the internal structure still comprised columnar crystals formed through layered growth. This might be attributed to incomplete heat input and untimely cooling during the spraying process [31]. Fig. 3(c) and 3(d) depicted the magnified images of the interfaces between the GZ surface layer and the $MoSi_2$ bonding layer, together with that between the bonding layer and the substrate. Minute cracks (with widths at the nanometer scale) persisted, and defects such as cracks existed at the interfaces. In Fig. 3(c), it was discerned that component segregation occurred in the $MoSi_2$ region. An EDS analysis was carried out on the region, and the relative content of each

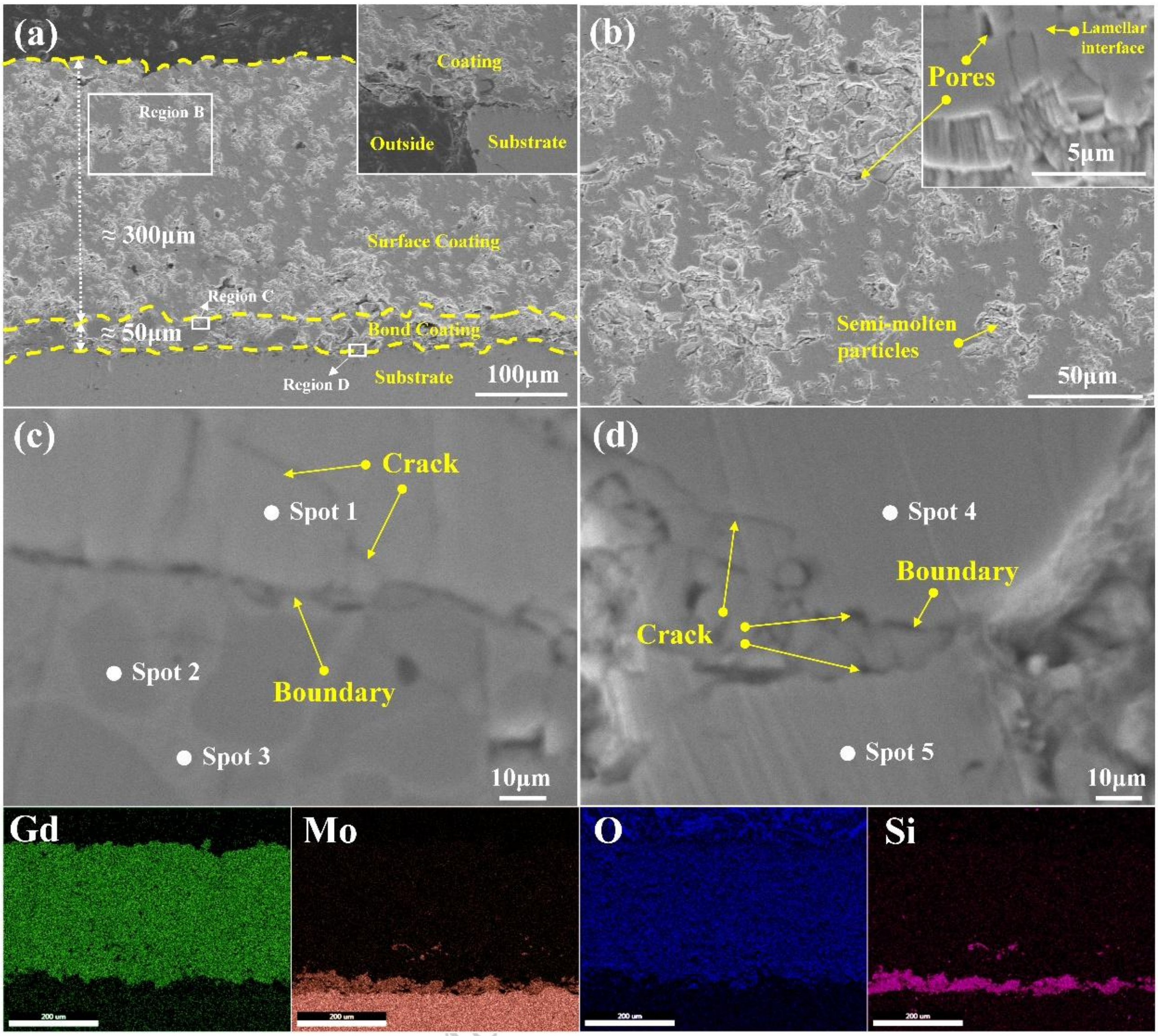

Fig. 3 Microstructure and structure analysis of the cross-section of $MoSi_2$-GZ coatings, as well as EDS analysis. (a) Complete cross-section of the coatings. (b) Magnified region. (c) Interface between GZ and $MoSi_2$ coatings. (d) Interface between $MoSi_2$ coatings and substrate.

Table 3 Element composition (at. %) for $MoSi_2$-GZ coatings.

Spot	Gd	Zr	O	Mo	Si
1	19.39	21.45	59.16	-	-
2	-	2.22	13.69	25.86	58.24
3	-	-	19.37	34.94	45.69
4	-	2.14	-	36.13	61.72
5	-	2.83	30.46	66.70	-

chemical component within the coatings was acquired. As indicated in Table 3, the proportion of Mo at points 3 and 4 in the $MoSi_2$ region was conspicuously higher than that at point 2. Moreover, since the coatings underwent oxidation during the spraying process, it was highly likely that points 3 and 4 were the enrichment zones of Mo oxides, and point 2 was the area where $MoSi_2$ and $MoSi_2$ were oxidized [32]. This also accounted for the reason why no compositional segregation occurred in the matrix and bonding layer regions in Fig. 3(d).

The XRD pattern of the $MoSi_2$-GZ coatings on Mo-Re alloy was shown in Fig. 4., which manifested the orientation of the $MoSi_2$ and $Gd_2Zr_2O_7$ grains and the intensity of the diffraction peaks after spraying. By integrating the information on the $MoSi_2$ and $Gd_2Zr_2O_7$ cards, it was observable that no conspicuous phase transition took place during the preparation of the coatings; however, there were still certain regions that turned amorphous [33]. On the whole, the GZ surface layer was successfully fabricated on the molybdenum-rhenium alloy surface without the interference of impurity phases.

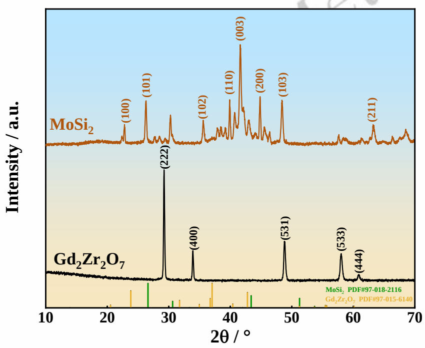

Fig.4 XRD patterns of $MoSi_2$-GZ coatings on Mo-Re alloy.

2.2 Mechanical properties of $MoSi_2$-GZ coatings

The indentation morphology of the $MoSi_2$-GZ composite coatings at various distances from the substrate was shown in Fig. 5, with Fig. 5(d) illustrating an indentation on the $MoSi_2$ coatings. It could be observed that cracks in the GZ coatings are shorter than those in the $MoSi_2$ coatings. The *c/a* ratios for GZ and $MoSi_2$ coatings were reported as 1.57-2.04 and 3.25 ± 0.22, respectively. The values within the range of 0.6-4.5 indicated that the fracture toughness calculation conditions in this study were consistent with those of the Evans & Wilshaw model, suggesting a correlation between anisotropic behavior and the accumulation of micro voids between thin films, which reduced actual contact area. In APS (Air plasma spraying) coatings, micropores preferentially accumulated at crack boundaries, making them the most susceptible regions to fracture [25]. Multiple and extensive cracking marks could also be observed near the coatings surface and interface in the indentation region. This was related to cracks at the interface and influenced by the degree of particle melting at the surface interface [27]. Despite re-preheating and post-spray treatment during GZ coatings on the $MoSi_2$ surface to reduce thermal stress, it could still be seen from the graph that particle melting was affected, resulting in weak interlocking bonding [29].

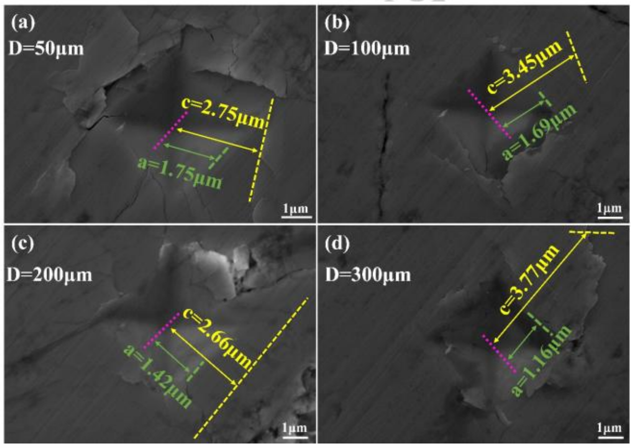

Fig.5 SEM image of the microhardness indentation on $MoSi_2$-GZ coatings. (a) 50 μm from the surface. (b) 100 μm from the surface. (a) 200 μm from the surface. (a) 300 μm from the surface.

The fracture toughness and microhardness of the composite coatings at various locations are obtained were shown in Fig. 6, according to formula (1) and the characterization of mechanical properties. Meanwhile, Table 4 presented the relevant mechanical properties of the coatings. From Fig. 6(a), it could be observed that the overall micro-hardness of the coatings ranges between 900 HV. At the interface between $MoSi_2$ and GZ coatings, there was no significant variation in hardness, indicating a lack of noticeable defects or porosity at this interface. However, it could be observed from the fracture toughness diagram that the fracture toughness of GZ and $MoSi_2$ coatings was 1.21-1.74 and 0.88 $MPa \cdot m^{1/2}$, respectively, indicating weaker crack propagation resistance in the $MoSi_2$ coatings. Compared to the GZ coatings, there are two main reasons for the lower toughness of the $MoSi_2$ coatings: (1) a lower degree of melting led to a reduction in anchor points for deposition splashing [16,28], which lowers bonding strength (the fracture occurred between $MoSi_2$ and GZ coatings rather than within the GZ coatings), thus providing a pathway for crack propagation along weak splashing boundaries; (2) an increase in porosity reduced the solid area carrying load and decreases fracture toughness.

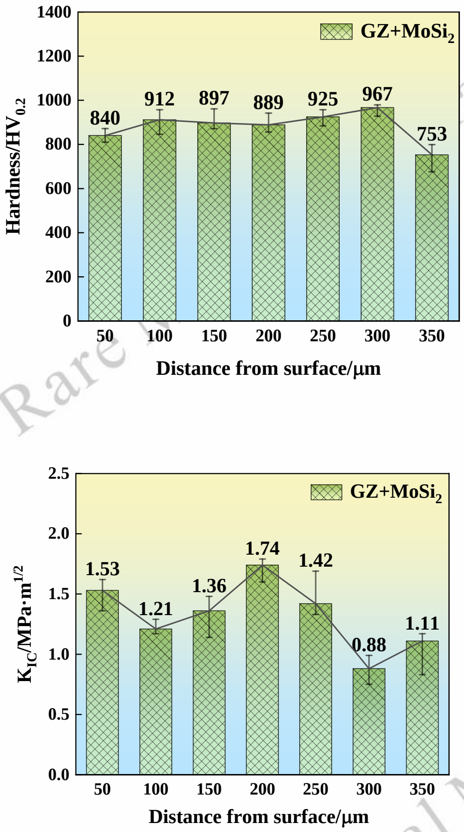

Fig.6 Micro-hardness and fracture toughness diagram of $MoSi_2$-GZ coatings.

Table 4 The coatings' thickness, porosity, bond strength and density of the test samples

Sample	Thickness, μm	Porosity (%)	Bond strength, MPa	Density （g/cm^3）
$MoSi_2$-GZ	350	39	25	6.823

2.3 Thermal properties of $MoSi_2$-GZ coatings.

The heat capacity of the coatings was shown in Fig. 7, increased from 0.518 to 0.601 J/K·g within the temperature range of 800-1200 ℃. The change in heat capacity was somewhat similar to that of the thermal expansion coefficient, rapidly increasing at low temperatures and then leveling off. This similarity could be attributed to its conformity with the Debye [20] model at low temperatures, where heat capacity was proportional to T^3 [17].

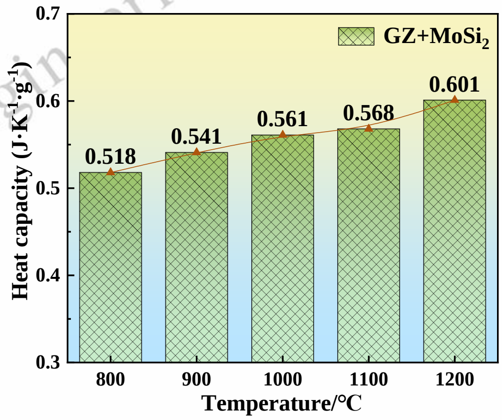

Fig.7 Heat capacity of $MoSi_2$-GZ coatings.

The thermal conductivity and thermal diffusion diagram of the coatings were shown in Fig. 8. The insulation performance was widely recognized to be related to the thermal conductivity of the coatings. At 1200℃, the composite coatings exhibited a thermal conductivity of 1.02 W/m·K, indicating good insulation properties for the $MoSi_2$-$Gd_2Zr_2O_7$ coatings. The low thermal conductivity of the composite coatings was related to the phase composition of the coatings and the high porosity (39%). For sprayed coatings, the thermal conductivity of GZ slightly increases from 800 to 1100°C and significantly increases between 1100-1200 ℃. Generally speaking, lattice defects such as vacancies play a crucial role in reducing thermal conductivity [32]. Among them, oxygen vacancies were considered the most essential lattice defects in ceramic materials, especially for ceramics with strong insulation capabilities [33]. This suggested that there were many oxygen vacancies present in the GZ coatings. In comparison, slight variation was observed in the thermal diffusivity of the coatings, fluctuating between 0.261-0.240 mm^2/s.

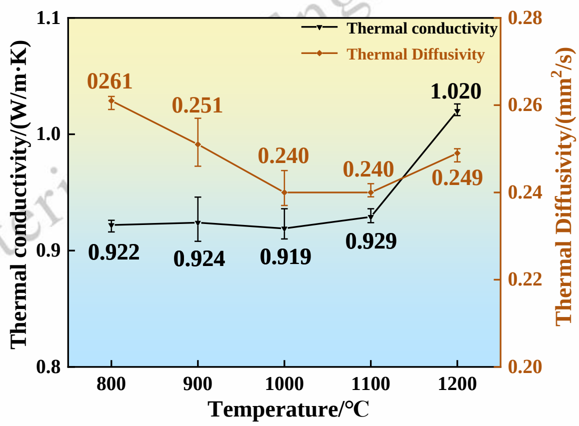

Fig.8 Thermal conductivity and diffusivity of $MoSi_2$-GZ coatings.

3 Conclusions

The microstructure, mechanical properties, and thermal properties of the $MoSi_2$-$Gd_2Zr_2O_7$ composite coatings prepared on a molybdenum-rhenium alloy substrate were analyzed in this study. The main conclusions were as follows:

1) By innovatively selecting the composition of the double-layer insulation coatings, the preparation process parameters and thickness of the composite coatings were determined. The $MoSi_2$-$Gd_2Zr_2O_7$ composite coatings exhibited high hardness (883.3 $HV_{0.2}$) and good adhesion without apparent cracks at the interface.

2) The melting effect of particles and cracks at the interface affected the fracture toughness at the coatings interface. Compared to a $MoSi_2$ coatings (0.88 $MPa\cdot m^{1/2}$), the $Gd_2Zr_2O_7$ coatings had higher fracture toughness (1.74 $MPa\cdot m^{1/2}$) and stronger resistance to crack propagation.

3) The prepared $MoSi_2$-$Gd_2Zr_2O_7$ composite coatings had high porosity (39%), low thermal conductivity (1.02 W/m·K at 1200 ℃), low thermal diffusivity (0.249 mm^2/s at 1200 ℃), and high oxygen vacancy concentration, resulting in a low thermal diffusivity and thermal conductivity ratio that ensured good insulation performance.

References

1 Chang Tian, Gao Xuanqiao, Lin Xiaohui, et al. *Rare Metal Materials and Engineering*[J], 2023, 52(1): 388-397.

2 Hailong Xu, Li Huang, Wen Zhang, et al. *Journal of Materials Research and Technology*[J], 2024, 30: 3877-3885.

3 Tyler D. Doležal, Nick A. Valverde, Jodie A. Yuwono, et al. *Materials & Design*[J], 2024, 244: 113226.

4 Lu Sun, MingJun Li, Li Chen, et al. *Acta Materialia*[J], 2024, 278: 120270.

5 Chunyu Cheng, Tiantian Lv, Bohao Song, et al. *Surfaces and Interfaces*[J], 2024, 53: 105050.

6 Hesamaldin Azizzadeh, Seyed Abdolkarim Sajjadi, Arezoo Sezavar. *Surface and Coatings Technology*[J], 2024, 482: 130701.

7 Chaoxi Shu, Jinshuang Wang, Xianjun Lu, et al. *Journal of the European Ceramic Society*[J], 2024, 44(4): 2537-2549.

8 ZHAO Hong-xu, DENG Chun-ming, FU Lang, et al. *Surface Technology*[J], 2022, 51(2): 116-128.

9 Mao Deng, Zhangyi Huang, Haomin Wang. *Scripta Materialia*[J], 2024, 242: 115945.

10 Xiangyang Liu, Yali Yu, Yi Han, et al. *Journal of the European Ceramic Society*[J], 2024, 44(15): 116736,

11 Kadir Mert Doleker, Abdullah Cahit Karaoglanli, Yasin Ozgurluk, et al. *Vacuum*[J], 2020, 177: 109401.

12 Haomin Wang, Yang Shi, Mao Deng, et al. *Ceramics International*[J], 2024, 50(17): 29268-29281.

13 Gao Yue, Xiping Guo, Yanqiang Qiao, et al. *Corrosion Science*[J], 2019, 153: 283-291.

14 Mao Jinyuan, Liu Min, Deng Chunming, et al. *Rare Metal Materials and Engineering*[J], 2016, 45(6): 1386-1390.

15 Fu Wenbin, Dai Mingjiang, Wei Chunbei, et al. *Rare Metal Materials and Engineering*[J], 2016, 45(10): 2543-2548.

16 Tao Fu, Yingyi Zhang, Fuqiang Shen, et al. *Materials Characterization*[J], 2022, 192: 112192.

17 Tao Fu, Zhichen Han, Yingyi Zhang, et al. *International Journal of Refractory Metals and Hard Materials*[J], 2024, 124: 106831.

18 Tao Fu, Yingyi Zhang, Luyu Chen, et al. *Journal of Materials Research and Technology*[J], 2024, 29: 491-503.

19 Yingyi Zhang, Tao Fu, Laihao Yu, et al. *Ceramics International*[J], 2022, 48: 20895-20904.

20 Alireza Sedighi, Mandana Adeli, Mansour Soltanieh. *Journal of Materials Research and Technology*[J], 2024, 30: 187-196.

21 Yingyi Zhang, Laiho Yu, Tao Fu, et al. *Surface and Coatings Technology*[J], 2022, 431: 128037.

22 Yingyi Zhang, Laihao Yu, Tao Fu, et al. *Journal of Alloys and Compounds*[J], 2022, 894: 162403.

23 Lu Zhu, Shipeng Zhang, Fan Ye, et al. Composites Part B: *Engineering*[J], 2024, 274: 111281.

24 Guoxun Sun, Weili Wang, Xiaoning Sun. *Ceramics International*[J], 2022, 48(6): 8589-8595.

25 Zaoyu Shen, Guanxi Liu, Yuqing Luo, et al. *Corrosion Science*[J], 2024, 226: 111641.

26 Brenda Juliet Martins Freitas, Guilherme Yuuki Koga, Siegfried Arneitz, et al. *Additive Manufacturing Letters*[J], 2024, 9: 100206.

27 Ji Shouchang, Li Jinglong, Yang Haiyu, et al. *Rare Metal Materials and Engineering*[J], 2023, 52(10): 3345-335.

28 Yangyang Pan, Dijuan Han, Shansong Huang, et al. *Surface and Coatings Technology*[J], 2023, 468: 129715.

29 Hesam Rezvani Sichani, Mehdi Salehi, Hossein Edris, et al. *Surface and Coatings Technology*[J], 2017, 309, 959-968.

30 D. Zois, A. Lekatou, M. Vardavoulias. *Surface and Coatings Technology*[J], 2009, 204: 15–27.

31 Lin Dong, Meijun Liu, Xiaofeng Zhang, et al. *Applied Surface Science*[J], 2021, 543: 148847.

32 Xin Wang, Tao Yang, Qingyu Li, et al. *Journal of the European Ceramic Society*[J], 2021, 41(4): 2415-2424.

33 ShuWei Yao, ChangJiu Li, JiaJia Tian, et al. *Acta Materialia*[J], 2016, 119: 9-25.

Mo-Re 合金表面 $MoSi_2$ 和 $Gd_2Zr_2O_7$ 复合涂层的显微组织和热性能

张冲[1,*]，汪欣[1]，徐海龙[1]，李延超[1]，马通祥[1]，王少鹏[1,*]

(1. 西北有色金属研究院，陕西 西安 710016)

摘 要：在钼铼合金热端部件表面制备了超高温双层隔热涂层，根据热膨胀系数及涂层功能设计并通过大气等离子喷涂技术完成了$MoSi_2$-$Gd_2Zr_2O_7$的双层隔热涂层的制备，并对其微观组织、力学性能及热学性能进行分析。结果表明：制备出的双层复合隔热涂层结合力良好，界面未出现明显裂纹。相较于$MoSi_2$涂层断裂韧性低（0.88 MPa·m$^{1/2}$），$Gd_2Zr_2O_7$涂层的断裂韧性（1.74 MPa·m$^{1/2}$）更高，抗裂纹传播能力更强。制备的$MoSi_2$-$Gd_2Zr_2O_7$复合涂层孔隙率高（39%）、导热系数低（1.02 W/m·K，1200℃）、热扩散系数低（0.249 mm^2/s，1200℃），氧空位浓度高，保证了良好的隔热性能。

关键词：$MoSi_2$-$Gd_2Zr_2O_7$涂层; 钼铼合金; TBCs; 隔热性能

作者简介：张冲，男，1996 年生，硕士，助理工程师，西北有色金属研究院腐蚀与防护研究所，陕西 西安 710016，电话：0086-29-86283410，E-mail: zhangchong0411@163.com